Impact of the Si/Al ratio on the ethanol/water coadsorption on MFI zeolites revealed using original quantitative IR approaches

Rita Zakhia Douaihy, Louwanda Lakiss, Mohamad El-Roz, Alexandre Vimont, Philippe Bazin

Impact of the Si/Al ratio on the ethanol/water coadsorption on MFI zeolites revealed using original quantitative IR approaches

Received 00th January 20xx,
Accepted 00th January 20xx

DOI: 10.1039/x0xx00000x

Rita Zakhia Douaihy,[a] Louwanda Lakiss ,[a] Mohamad El-Roz, [a] Alexandre Vimont [a] and Philippe Bazin [*,a].

Advanced IR vibrational spectroscopic techniques, e.g., coupled gravimetric-IR surface analyzer (AGIR) and high-throughput in-situ IR cell (CARROUCELL), have been used for the quantitative studies of the adsorption and co-adsorption of ethanol and water on MFI zeolites with different Si/Al ratios. At low partial pressures, the unary water adsorption experiments suggest that the amount of adsorbed water results mainly from the preferential adsorption on Bronsted acid sites in tetrameric clusters. By contrast, adsorption of EtOH occurs on both silanol groups and Bronsted acid sites (BAS), while the effect of the Si/Al ratio is only observed at relatively low partial pressures. The molar absorption coefficients of adsorbed ethanol and water were determined and found to be independent of the Si/Al and are not affected during the coadsorption of ethanol and water. Their use allows to obtain the exact quantity of each adsorbate specie in the binary system. The effect of the Si/Al ratio on the ethanol adsorption capacity is also investigated and directs the choice of the separation membrane for ethanol purification.

1. Introduction

The recent energy and climate crisis have pushed researchers to find alternatives for fossil fuels [1]. Countries have shifted to environmentally friendly and more efficient biofuels to minimize the extraction of fossil fuels and greenhouse gases [2, 3]. Among the various biofuels and bio-alcohols, bioethanol has gained significant interest due to its presence in the liquid phase, its use as a partial replacement for gasoline, and its facile transportation [4-6]. It can be produced from different sources ranging from food renewable sources such as corn starch and sugarcanes to non-food renewable sources, including the organic fraction of municipal solid waste and lignocellulosic biomasses [7, 8]. Several techniques are applied to synthesize bioethanol, yet the main challenge is separating ethanol from ethanol/water mixture [9]. Bioethanol should be anhydrous to be used as a replacement for gasoline [6, 10]. On an industrial scale, conventional distillation and separation processes are considered costly, energy, and time-consuming due to the necessity to overcome the azeotrope barrier [11]. Therefore, other separation methods (pervaporation [12], etc.) were elucidated to separate the ethanol-water mixture beyond the azeotropic mixture based on the adsorption on porous materials [10, 13]. Among them, zeolites are excellent candidates. They are used in catalysis, adsorption, and separation of gaseous mixtures and biotechnologies [14-16], due to their high tunable porosities, tunable characteristics, and high chemical and thermal stabilities [14, 17]. Adsorption of ethanol (EtOH) on zeolitic materials has been extensively studied using experimental or theoretical approaches [10, 18-27]. Silica zeolites with high silica contents present high selectivity for alcohols towards the water, contrary to zeolites with higher alumina content [21, 28]. Then, MFI zeolites have attracted attention due to the possibility of varying the aluminum content easily during the synthesis, allowing for tuning the hydrophobic/hydrophilic properties [29]. The organophilic nature of MFI zeolites was confirmed by Gómez-Álvarez et al. [30] and Zhang et al. [31]. They concluded that no matter the Si/Al ratio of the MFI zeolites, the same behavior towards ethanol was observed. This was not the case when adsorbing water, where water uptake decreased with the increase of the Si/Al ratio [32]. Experimental data relative to co-adsorption experiments (selectivity) are scarce [30]. Different techniques were implemented to study the adsorption and coadsorption of water and/or ethanol, such as volumetric and gravimetric measurements and pulsed-field gradient (PFG)-nuclear magnetic resonance (NMR) [31, 33-35]. They necessitate long-time data acquisitions and quantifying each adsorbate during their coadsorption could be very challenging. Few studies reported the use of IR spectroscopy [36, 37]. In fact, IR spectroscopy can be used to determine the nature and the quantities of the adsorbed species when coupled with gravimetric analyses [13, 38].

The aim of this work is to study quantitatively the adsorption and co-adsorption of ethanol and water vapors on a series of MFI zeolites with various Si/Al ratios (from 11 to infinite (silicalite)) using (i) home-made coupled IR-gravimetry apparatus (namely AGIR) and a new multi-sample (up to 12 samples) in situ cell (namely CARROUCELL). This latter allows us to obtain in a reasonable time-acquisitions some sets of quantitative co-adsorption data for large water and ethanol vapor phase concentrations (P/P_0=0.006-0.65).

2. Experimental section

2.1. Materials:

A series of MFI zeolites with different Si/Al ratios was used in this work. The MFI-X systematic notation was used to name the zeolitic materials with X for the Si/Al molar ratio. Silicalite-1 was provided by Lakiss *et al.* and synthesized according to the procedure in reference [39]. MFI-75 and MFI-38 were synthesized according to ref [40]; MFI-45 was a commercially synthesized zeolite by Clariant (formerly Süd Chemie), MFI-25 from Qin *et al.*'s work [41]. MFI-15 and MFI-11 were provided by IFP, synthesized without the template, and in the presence of pre-synthesized germinal zeolites, respectively.

[a] *Normandie Université, ENSICAEN, UNICAEN, CNRS, Laboratoire Catalyse et Spectrochimie, 14050 Caen, France*
* Corresponding author
Electronic Supplementary Information (ESI) available: [details of any supplementary information available should be included here]. See DOI: 10.1039/x0xx00000x

2.2. Characterization techniques:

The PXRD patterns of the zeolites were recorded on a PANalytical X'Pert Pro diffractometer with an average Cu Kα radiation (λ = 1.5418 Å). The θ-2θ scans were recorded in the range of 2θ between 5° and 50° and a step size of ~ 0.0167°. The main characteristic peaks of the MFI structure are present on all the patterns without any additional peaks, confirming the purity of the samples.

The Si/Al ratio was determined from the elemental analysis using inductively coupled plasma spectroscopy coupled with mass spectrometry. The powder was dissolved in a mixture of aqua regia ($HCl+HNO_3$) and hydrofluoric acid (HF) at 90 °C. HF was then neutralized using boric acid (H_3BO_4). The mass spectrum of the diluted analyte solution was recorded after ionizing the solution with a high-energy Ar-plasma.

Nitrogen sorption isotherms at 77 K have been recorded on Micrometrics ASAP 2020 volumetric adsorption analyzer after degassing the samples at 350 °C for 12 hours. The specific surface areas are determined from the BET equation. The total pore volumes and the external surface areas are calculated from the *t*-plot method.

The morphology of zeolite crystals was investigated using scanning electron microscopy (SEM). SEM images were recorded on a TESCAN Mira field-emission scanning microscope at 20 kV. Before recording the images, the powder was dispersed on carbon tape and coated with platinum.

2.3. In situ IR Spectroscopy:

Self-supported pellets of pressed powder of each zeolite (~20 mg, 10^7 Pa/cm², S = 2.0 cm²) are mounted in an in-situ IR cell equipped with KBr windows connected to a Nicolet 6700 IR spectrophotometer. The spectrometer is equipped with a DTGS detector and an extended-KBr beam splitter. IR spectra were recorded in the region between 400 and 5500 cm^{-1} with a resolution of 4 cm^{-1} and 128 scans/spectrum [38]. The in-situ IR cell used in this work is the PELICAEN cell which is the latest version developed by the LCS laboratory to improve sample temperature control and automate the main functions (change of positions of the sample from the oven to the IR beam, acquisition of the IR spectra). The PELICAEN is mainly made of quartz. The sample holder is designed with a platinum wire. The heating system (up to 700 °C) is a tubular furnace from ERALY (France). A thermocouple is positioned inside the cell near the sample to perfectly control its temperature, particularly when placed under a vacuum (low thermal conductivity condition). An additional gauge is added to the IR cell to precisely measure the pressure inside the chamber. For the IR spectroscopic evaluation of the properties of porous materials, the addition of probe molecules can also be done gradually and quantitatively via a small, calibrated volume (approximately 2.0 cm^3) positioned at the front side of the cell. The PELICAEN cell is connected to the vacuum apparatus to treat the sample and introduce the gaseous phase when necessary. In this work, zeolites were activated at 400 °C (heating rate 2 °C.min^{-1}) under a vacuum (around 10^{-5} Torr) for 5 hours.

2.4. Method for the determination of the molar absorption coefficients of adsorbed ethanol and water:

The AGIR technique allows to measure the gravimetric data and records the corresponding IR spectra simultaneously [13, 38, 42]. Therefore, the AGIR is very well suited to evaluate the molar absorption coefficients of the bands associated with the vibration modes of the adsorbed molecules. Note that these coefficients are essential for quantitative investigations. The setup is connected to a mass spectrometer to monitor the outlet flow of the adsorbates in the gas phase (Pfeiffer Omnistar GSD301). The experiments were conducted on a self-supported pellet of the pressed powder of the adsorbent (~20 mg, 10^7 Pa/cm², S = 2.0 cm²), previously activated at 400 °C (heating rate 0.6 °C. min^{-1}) under a gas flow (20 $cm^3.min^{-1}$) of a mixture of argon and oxygen (20 %). IR spectra were recorded using a Nicolet 6700 spectrometer outfitted with liquid nitrogen cooled MCT detector (mercury, cadmium, and tellurium detector) at a resolution of 4 cm^{-1} in the spectral region between 600 cm^{-1} and 6000 cm^{-1}. The mass of the sample was recorded using a microbalance (accuracy= 0.1 µg), and the corresponding IR spectra were registered after the equilibrium state of H_2O and EtOH concentration. The steady-state was determined by both the absence of change in mass and the intensity of the characteristic band of each adsorbate.

2.5. Adsorption and coadsorption of ethanol and water using the CARROUCELL high-throughput IR cell:

To reduce the experimental time drastically due to the high number of samples and different partial pressure points of H_2O and C_2H_5OH, the coadsorption measurements were carried out on the CARROUCELL apparatus [38]. This sophisticated IR apparatus developed in the laboratory allows us to do the same experimental conditions on twelve samples simultaneously (all samples are positioned in the same analysis chamber). The setup is formed of an *in-situ* IR cell, attached to a vacuum system, and adapted for 12 samples of self-supported pellets formed of a pressed powder (~20 mg, 10^7 Pa/cm², S = 2.0 cm²). The background and the gas phase spectra are recorded between each sample and are automatically subtracted. In this work, CARROUCELL is adapted for experiments under gas flow, so experimental conditions are similar to that of the AGIR setup. Upstream of the adsorption sequences, the zeolites are activated at 400 °C under an argon flow. At first, a water concentration was introduced to the cell at RT, followed by the adsorption of increasing ethanol concentrations after reaching equilibrium. The equilibrium after ethanol and water adsorption is determined between two consecutive IR spectra, where no change in the characteristic vibrational bands of the adsorbates is observed. The coadsorption experiments were conducted at 25 °C at different water concentrations, ranging between P/P_0 = 0.016 and 0.64. As for the partial pressure of ethanol, it increases from 0.006 to 0.65.

3. Results and discussion

3.1. Structural and textural properties:

The textural porosities of the zeolites are investigated using nitrogen adsorption/desorption and are summarized in **Table 1** after determining their Si/Al ratio and confirming their purity from the PXRD patterns **(Figure S1 (A))**. The N_2 isotherms are represented in **Figure S1 (B)** and correspond to type I isotherms, characteristic of microporous zeolites [43]. The BET surface areas and the micropore volumes of the different zeolites vary in the same range. Zeolites are then characterized using IR spectroscopy, and the corresponding IR spectra are represented in the stretching OH spectral region of the between 3800 and 3500 cm^{-1} **(Figure S2)**. Two major peaks are observed : the first ν_{OH} band at 3744 cm^{-1} corresponds to the silanol groups located on the outer surface of the crystallite [44]. The second, situated at 3610 cm^{-1} and absent in the IR spectrum of Silicalite-1 (**Figure S2**, spectrum (a)), is attributed to structural bridged Si(OH)Al, namely Bronsted acid sites (BAS) [45]. The absence of an additional vibrational band near 3665 cm^{-1} indicates that no vibrations of the OH groups bound to the extra-framework Al species are present [46, 47].

Moreover, the morphology of the crystals is determined using scanning electron microscopy. SEM images (**Figure 1**) reveal aggregation of nanospheres of a size ranging between 30 to 100 nm for all zeolites. The SEM image of MFI-11 shows an agglomeration of nano-sheets of less than 100 nm.

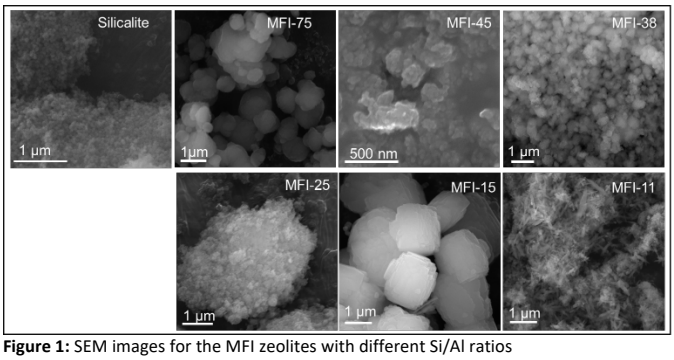

Figure 1: SEM images for the MFI zeolites with different Si/Al ratios

Table 1: Si/Al ratio determined by elemental analysis, textural properties tested by N_2 adsorption/desorption at 77 K and accessibility of acid sites of different MFI zeolites tested by pyridine adsorption at 150 °C.

	Silicalite	MFI-75	MFI-45	MFI-38	MFI-25	MFI-15	MFI-11
Si/Al ratio [a]	∞	75	45	38	25	15	11
S_{BET} [b] (m^2/g)	502	421	452	423	475	413	444
Micropore volume [c] (cm^3/g)	0.158	0.157	0.153	0.155	0.156	0.166	0.162
Number of Al/ unit cell	0	1.3	2.1	2.5	3.7	6.0	8.0
n Lewis acid sites [d] (µmol/g)	0	12	44	46	48	51	34
n BAS (µmol/g) [e]	0	145	190	157	270	524	712

[a] Calculated from ICP, [b] BET surface area, [c] *t*-plot, [d] $\varepsilon_{1455} = 1.8\ \text{cm.}\,\mu\text{mol}^{-1}$ [38], [e] $\varepsilon_{1547} = 1.4 \pm 0.2\ \text{cm.}\,\mu\text{mol}^{-1}$.

3.2. Accessibility of acid sites:

The concentrations of both Bronsted and Lewis acid sites have been determined for each zeolite from Pyridine adsorption followed by IR spectroscopy. An excess of Pyridine sufficient to neutralize all acid sites was established in the IR cell at 150 °C (1 Torr at equilibrium pressure), followed by an evacuation (secondary vacuum) at the same temperature to remove the gaseous and physisorbed probe molecules. Finally, the corresponding spectra were recorded at RT to determine the number of acidic sites of each zeolite using the area of the 1547 cm^{-1} band of pyridinium ions (Bronsted) and the 1455 cm^{-1} band of Pyridine coordinatively bonded to Lewis sites by applying their respective molar absorption coefficients. The subtraction spectra (before and after Pyridine adsorption) are represented in **Figure 2 (A)** in the spectral region between 1700 and 1400 cm^{-1}. The quantities of adsorbed PyH^+ and PyL formed on the acidic sites are summarized in **Table 1** using the calculated molar absorption coefficients for MFI zeolite. The number of BAS is plotted as a function of the number of Al calculated per unit cell (**Figure 2 (B)**). The amount of Bronsted (BAS) acid sites clearly increases proportionally with the number of the Al content per unit cell. However, the amount of Lewis acid sites remains relatively low compared to that of the BAS.

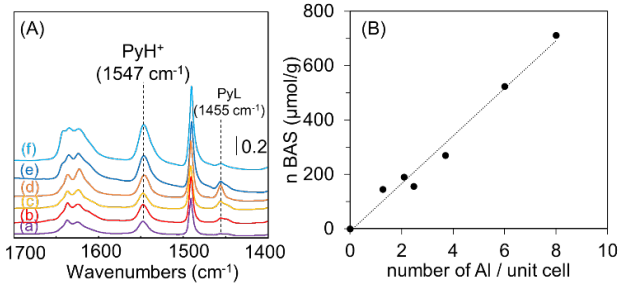

Figure 2: (A) Subtraction IR spectra before and after Pyridine adsorption for MFI-75 ((a), purple), MFI-45 ((b), red), MFI-38 ((c), yellow), MFI-25 ((d), orange), MFI-15 ((e), dark blue) and MFI-11 ((f), light blue). The spectra were collected at RT after Pyridine adsorption at 150 °C and normalized to the mass of the pellet (20 mg). (B) Evolution of the amount of Bronsted acid sites as a function of the Al content per unit cell.

3.3. Determination of the molar absorption coefficients of adsorbed ethanol $\varepsilon(\frac{1450\ cm^{-1}}{\delta_{EtOH}})$ and water and $\varepsilon(\frac{1630\ cm^{-1}}{\delta_{H_2O}})$:

Determining the molar absorption coefficients relative to the adsorbed water and alcohol is essential to convert the IR spectra into quantitative data. For this purpose, the adsorption of ethanol and water is investigated using IR spectroscopy and conducted on the AGIR setup for all MFI zeolites. The experiments were repeated two times to check the reproducibility.

Typical IR spectra recorded at room temperature of adsorbed ethanol and water are displayed in **Figure 3 (A)** for the MFI-45 sample. The main characteristic vibrational bands of adsorbed ethanol are situated at 3000-2800 cm^{-1}, 1500-1350 cm^{-1}, and 880 cm^{-1} and are attributed to ν_{CH} , δ_{CH} and $\nu_{s\,(CCO)}$ modes, respectively. In the present study, only the band of ethanol at 1450 cm^{-1} (δas_{CH_3} mode) is considered: the ν_{CH} bands of ethanol at 3000-2800 cm^{-1} are intense, and the area is only measurable at low alcohol pressures, whereas the area of the band at 880 cm^{-1} is difficult to assess precisely due to the strong fluctuations and perturbation of the baseline ("U" shape curve) by the structural bands of the zeolites.

In the case of H_2O, the main spectral bands observed at ~1630 cm^{-1} and ~5200 cm^{-1} are respectively assigned to the δ_{H_2O} and $(\delta + \nu)_{H_2O}$ vibration modes. Only the band at 1630 cm^{-1} is considered since the signal-to-noise ratio at ~5200 cm^{-1} at low water pressure is too low for accurate integration of the band area.

The area of the characteristic band of ethanol ($\delta_{EtOH}^{1450\ cm^{-1}}$) (**Figure 3 (B)**) at 1450 cm^{-1} and that of water ($\delta_{H_2O}^{1630\ cm^{-1}}$) situated at 1630 cm^{-1} (**Figure 3 (C)**) are plotted as a function of the quantities of the adsorbed species determined by gravimetric measurements. For the overall zeolites, molar absorption coefficients (ε (cm.µmol^{-1})) are thus determined as proportional to the slope of the plot (= double the slope to take into account the area of the pellet) according to the Beer-Lambert law (**equation 1**):

$$A = \varepsilon.l.c = \varepsilon.l.\frac{n}{V} = \varepsilon.l.\frac{n}{l.S} = \varepsilon.\frac{n}{S} \qquad \textbf{(equation 1)}$$

with A (cm^{-1}) the integrated area of the band, ε (cm.µmol^{-1}) the molar absorption coefficient, l (cm) the optical pathway, c (µmol per volume unity) the concentration of the adsorbate, V (cm^3) the volume of the pellet, S (= 2.0 cm^2) the surface of the pellet and n (µmol) the amount of the adsorbate.

From the slope of the straight line, an average value for the molar absorption coefficients $\varepsilon(\frac{1450\ cm^{-1}}{\delta_{EtOH}})$ and $\varepsilon(\frac{1630\ cm^{-1}}{\delta_{H_2O}})$ is calculated and found to be equal to 0.14 ± 0.01 and 1.29 ± 0.06 cm.µmol^{-1}, respectively. These values are found to be independent of the Si/Al ratio of the MFI zeolites.

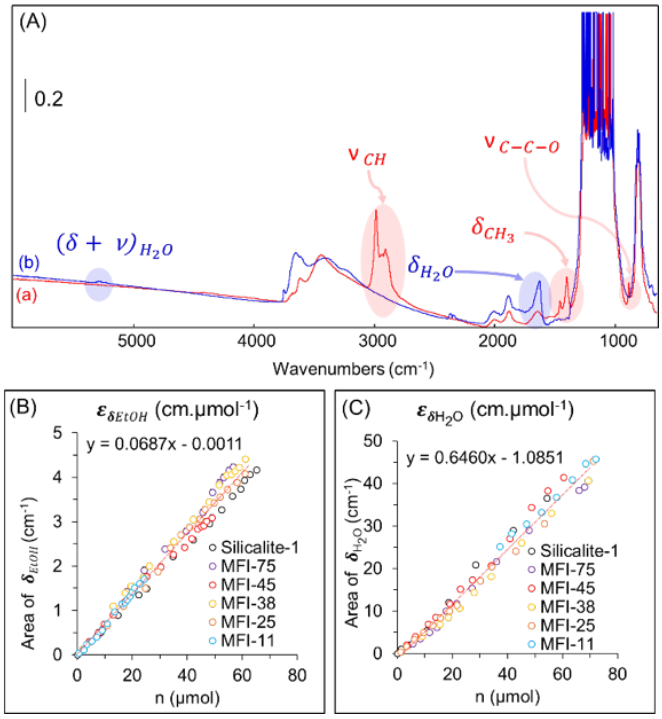

Figure 3: (A) IR spectra of MFI-45 with the characteristic bands after ethanol ((a)-red) and water ((b)-blue) adsorption at RT. Evolution of the area of the characteristic band of (B) ethanol (1450 cm^{-1}) and (C) water (1630 cm^{-1}) as a function of the quantities adsorbed on Silicalite-1 (black), MFI-75 (purple), MFI-45 (red), MFI-38 (yellow), MFI-25 (orange) and MFI-11 (light blue).

3.4. Adsorption of ethanol or water on MFI-45:

Ethanol and water are adsorbed separately on MFI-45. MFI-45 was chosen as reference material to present in detail the spectroscopic study of water and ethanol adsorptions considering its intermediate Si/Al ratio (concomitant presence of Si-OH and BAS sites).

3.4.1. Adsorption isotherm of ethanol

The isotherms of ethanol adsorption with the corresponding IR spectra are represented in **Figure 4**; at low ethanol partial pressures ($P/P_0 < 0.01$), ethanol is adsorbed to fill the porosity of the MFI zeolite (**Figure 4 (A)-curve (a)**). The corresponding IR spectra in the OH region are represented in **Figure 4 (B)** and reveal that the ν_{OH} band at 3610 cm^{-1}, characteristic of the BAS, disappears immediately after the first equilibrium pressure ($P/P_0 = 0.0065$). This observation agrees with the results obtained by Alexopoulos et al. [27]. With the increase of the partial pressure, the quantity of adsorbed ethanol on MFI-45 increases to reach a maximum of around 2500 µmol/g at $P/P_0 = 0.65$. As suggested by Gómez-Álvarez *et al.*, the zigzag channels of the MFI structure are responsible for the high adsorption capacity toward ethanol [30]. The ethanol adsorption on MFI-45 occurs in a monolayer adsorption model, previously described in the literature by a Langmuir model [31]. However, the concomitant decrease in the intensity of ν_{OH} at 3744 cm^{-1} assigned to external silanol groups at $P/P_0 = 0.0065$ shows that ethanol adsorption takes place also on the outer surface of the zeolite structure. This agrees with the results stating that ethanol highly interacts with the silanol groups of the MFI zeolites in the membrane[48, 49].

To elucidate the role of BAS on the adsorption sites of ethanol on MFI zeolites, ethanol is adsorbed on MFI-45 previously treated with Lutidine, a basic probe molecule well-known to poison BAS of the zeolites, specifically [50, 51]. The spectra of MFI-45 before and after Lutidine adsorption (**Figure S3**) show that the characteristic band of the Bronsted acid sites at 3610 cm^{-1} disappears after introducing Lutidine. In contrast, the bands of Lutidinium at 1630 and 1650 cm^{-1} are well detected, showing the blockage of the BAS before ethanol adsorption. The gravimetric isotherms after ethanol adsorption in the presence of Lutidine and the corresponding IR spectra in the OH region are represented in (**Figure 4**) and compared to the gravimetric adsorption isotherms of the Lutidine free parent MFI zeolite. A slight decrease in the ethanol adsorbed quantity was observed (around 20 %) (**Figure 4 (A) – curve (b)**). After adsorbing ethanol, the characteristic vibrational band at 3744 cm^{-1} is highly affected at very low ethanol partial pressures in the presence of Lutidine (**Figure 4 (C)**). Its intensity decreases with the increase of the partial pressure. Based on these results, we can assume that the adsorption of ethanol takes place on the silanol groups since a slight decrease in the quantity of adsorbed ethanol is observed after blocking the BAS. In addition, the number of adsorbed ethanol molecules per Bronsted acid

site could be determined from the subtraction between the gravimetric isotherms before and after adsorbing Lutidine. The difference suggests that two ethanol molecules are adsorbed on a BAS, agreeing with the data in the literature [27] (for example, for P/P_0=0.65, the difference in adsorbed EtOH is 468 µmol/g, and the number of BAS is equal to 235 µmol/g, i.e., an EtOH / BAS ratio equal to ~2).

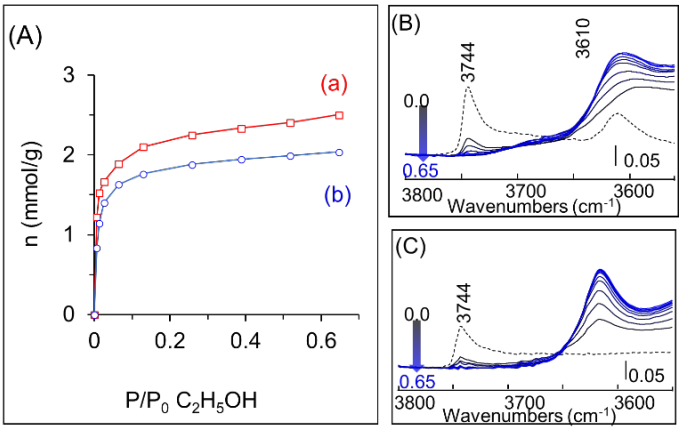

Figure 4: (A)Gravimetric adsorption isotherms after C_2H_5OH adsorption on MFI-45 at RT ((a)-red) without and ((b)-blue) with pre-adsorbed Lutidine. Evolution of the corresponding IR spectra at increasing partial pressures of C_2H_5OH in the spectral regions between the OH stretching region (3800-3550 cm^{-1}) (B) without and (C) with pre-adsorbed Lutidine. The dashed spectra correspond to the initial spectra after activation at RT and before adsorption. Spectra are normalized to 20 mg of zeolite.

3.4.2. Adsorption isotherm of water

The isotherm of water adsorption is displayed in **Figure 5 (A)-curve (a),** and the corresponding IR spectra are represented in **Figure 5 (B)**. The band of the BAS at 3610 cm^{-1} disappears at the first water uptake (P/P_0 = 0.01), whereas the intensity of the SiOH groups at 3744 cm^{-1} is weakly affected and subsequently decreases significantly only for P/P_0 up to 0.04. This suggests that water molecules interacts specifically with BAS at low partial pressure [52]. While the sensitivity of the ν_{OH} band of BAS upon water and ethanol adsorption is similar, this is not the case for the ν_{OH} band of silanol, much more affected upon ethanol adsorption [27, 31, 53]. This can be explained considering the difference of affinity toward ethanol and water, e.g., the enthalpies of adsorption. The enthalpy of ethanol adsorption is higher than that of water and is characterized by two plateaus. Whereas that of water is characterized by a single plateau attributed to the clustering of water molecules [54]. Water molecules are first adsorbed on the Bronsted acid sites, and then strong interactions occur between the adsorbed water molecules and the second water molecules [55].

Water adsorption sites are further studied after adsorbing Lutidine. The gravimetric isotherm of water adsorption on MFI-45 with pre-adsorbed Lutidine and the corresponding IR spectra in the OH region are represented in **Figures 5 (A) and (C)**. By comparing the gravimetric isotherms, the quantity of adsorbed water on MFI-45 without Lutidine is more important than on MFI-45 filled with Lutidine. After adsorbing water, a minor decrease of the vibrational band at 3744 cm^{-1} is observed at water partial pressure $0 < P/P_0 < 0.16$. At higher partial pressures, an important decrease in the intensity of the characteristic bands of the silanols is observed. These observations allow us to confirm the adsorption of water molecules on BAS and the weak interactions with the silanol groups [36, 56]. Moreover, the difference between the adsorption isotherms of water with and without Lutidine demonstrates that four water molecules are adsorbed on one BAS at low water partial pressure ($P/P_0 \leq 0.02$). For example, for P/P_0=0.02, the difference in adsorbed water is 931 µmol/g, and the number of BAS is equal to 235 µmol/g, i.e., an H_2O / BAS ratio equal ~ 4). Similar results were obtained by Olson et al. [32, 57] and Bolis et al. [56].

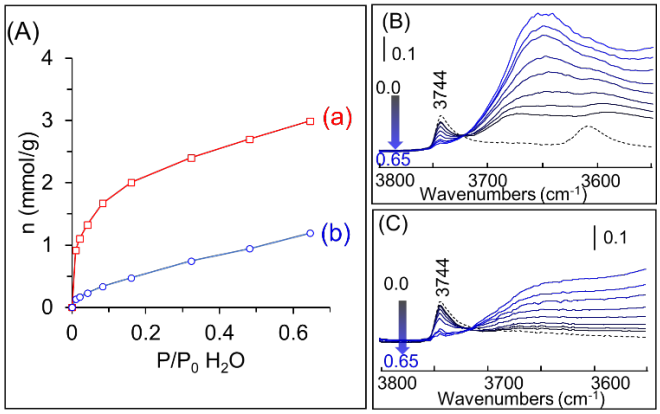

Figure 5: Gravimetric adsorption isotherms after H_2O adsorption on MFI-45 at RT ((a)-red) without and ((b)-blue) with pre-adsorbed Lutidine (A). Evolution of the corresponding IR spectra at increasing partial pressures of H_2O in the spectral regions between OH stretching region (3800-3550 cm^{-1}) (B) without and (C) with pre-adsorbed Lutidine. The dashed spectra correspond to the initial spectra after activation at RT and before H_2O adsorption. Spectra are normalized to 20 mg of zeolite.

3.5. Adsorption of ethanol or water on MFI zeolites with different Si/Al ratios

The adsorption of ethanol and water is further investigated on MFI with different Si/Al ratios. The gravimetric isotherms of ethanol and water are determined from the AGIR setup and are represented in **Figure 6.** The corresponding IR spectra at fixed partial pressures are represented in **Figure S4**. The quantity of adsorbed ethanol increases until reaching an equilibrium at P/P_0 = 0.3. At P/P_0 > 0.3, the quantity of adsorbed ethanol increases slightly to reach a maximum ranging between 2400 and 3100 µmol/g. Ethanol adsorption isotherms follow a similar adsorption type regardless of the Si/Al ratio. A Langmuir-like model can be observed, where the organophilic character of MFI zeolites is responsible for the monolayer adsorption of ethanol. These results agree with the previous results described in the literature [31]. The effect of the Si/Al ratio is mainly observed at low ethanol partial pressures (P/P_0 < 0.01) (**Figure 6 (C)**), where zeolites with low Si/Al ratio adsorb the highest amount ethanol amount.

A different trend is observed after water adsorption (**Figures 6 (B)** and **(D)**). First, all zeolites exhibit a Freundlich-like isotherm upon water adsorption, where different layers of adsorbed water are formed [55]. On silicalite-1 and MFI zeolites with relatively high Si/Al ratios, the quantity of adsorbed water varies in the same range between 2700 and 3300 µmol/g. However, at a lower Si/Al ratio, for MFI-25 and MFI-11, a significant increase in water adsorption capacity is observed. The adsorbed water quantity at P/P_0 = 0.64 reaches 6100 µmol/g. These differences are attributed to the change of the hydrophobic character of zeolite due to the presence of Al in the framework [31, 32]. The presence of Al is responsible for creating Bronsted acid sites in the framework (**Table 1**), considered as the adsorption sites for water. As a result, the hydrophobic character of the zeolite decreases, increasing, thus the adsorption capacity of water. This adsorption model is also confirmed by the linear correlation between the number of BAS determined by Pyridine adsorption and the quantity of adsorbed water at very low partial pressures (P/P_0= 0.0065) (**Figure S5**). The linear correlation between the quantities of these adsorbed species and the number of Bronsted acid sites determined by pyridine adsorption allows us to determine the number of adsorbed molecules per acid site for each adsorbate at each partial pressure. The slope of the linear correlation indicates that four water molecules are adsorbed at high partial pressure on the Bronsted acid sites. These results are consistent with the previously demonstrated results on MFI-45 after adsorption of Lutidine. Whereas for ethanol, the number of adsorbed ethanol is only determined upon Lutidine adsorption (two molecules per BAS).

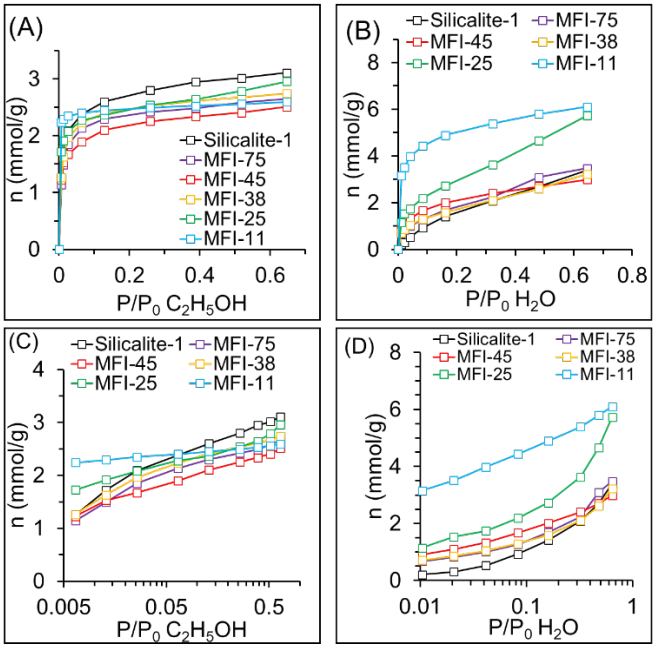

Figure 6: Adsorption isotherms of (A) ethanol and (B) water on Silicalite-1 (black), MFI-75 (purple), MFI-45 (red), MFI-38 (yellow), MFI-25 green, and MFI-11 (light blue). Semi-log plot of the adsorption isotherms of (C) ethanol and (D) water.

3.6. Coadsorption of ethanol and water on MFI zeolites with different Si/Al ratios:

3.6.1. Validation of the $\varepsilon(^{1450\ cm^{-1}}_{\delta_{EtOH}})$ and $\varepsilon(^{1630\ cm^{-1}}_{\delta_{H_2O}})$ values for coadsorption experiments: comparison between AGIR and CARROUCELL setups

The coadsorption of ethanol and water on the MFI zeolites with different Si/Al ratios was conducted on the CARROUCELL setup, previously described in the experimental section. A single experiment was conducted first on the AGIR setup on MFI-45 to confirm that the molar absorption coefficients determined during pure ethanol and water adsorptions do not change during their coadsorption. Water is initially adsorbed on the zeolite, and when the equilibrium is reached, the gas flow is enriched with an increasing concentration of ethanol. IR spectra of MFI-45 recorded on the CARROUCELL for different P/P_0 of C_2H_5OH, and at a fixed H_2O concentration (P/P_0 = 0.32) are reported (**Figure 7(B)**). Initially, in the absence of EtOH, only the peak at ~1630 cm^{-1} characteristic of adsorbed water is present. Subsequently, the step-by-step increase in the partial pressure P/P_0 of C_2H_5OH leads to a decrease in the intensity of the δ_{H_2O} band and to the concomitant increase of the characteristic bands of the adsorbed alcohol, in particular, the one positioned at 1450 cm^{-1}. The molar absorption coefficients previously determined from the AGIR setup are used to determine the quantities of each adsorbed specie from the IR spectra recorded on the CARROUCELL. Finally, the calculated total quantity of ethanol and water adsorbed on the zeolite via the CARROUCELL is compared to the mass uptake recorded with the microbalance of the AGIR setup (**Figure 7(A)**). The results show that the quantities of adsorbed ethanol and water are similar, as illustrated by the linear correlation obtained between the total adsorbed quantities determined by the AGIR tool and the CARROUCELL via the molar absorption coefficients, respectively (inset **Figure 7(A)**). Thus, we conclude that the molar absorption coefficient of each adsorbate is not significantly affected by the presence of the second specie. Consequently, the CARROUCELL set-up can be used to drastically reduce the experimental time while rigorously reproducing the same conditions (temperature and pressure) since the experiment is carried out simultaneously for all the samples positioned in the same environmental environment chamber.

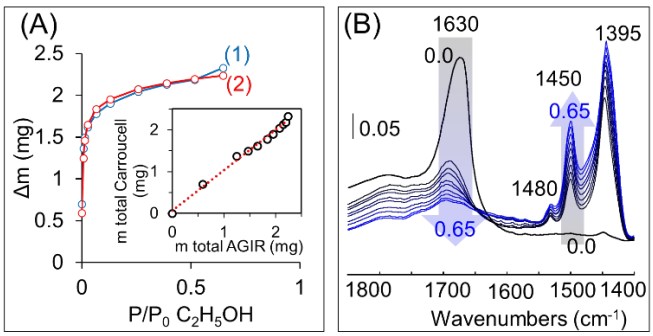

Figure 7: (A) Mass variation (Δm, mg) as a function of increasing P/P_0 of C_2H_5OH determined using the Carroucell ((1), blue)) and using AGIR ((2), red). (B) Evolution of IR spectra of MFI-45 recorded on the Carroucell for increasing P/P_0 of C_2H_5OH and a fixed H_2O concentration (P/P_0 = 0.32). The spectra correspond to the subtracted spectrum between the spectra after activation recorded at RT and the successive spectra recorded at RT at equilibrium after C_2H_5OH/H_2O adsorption. Inset of (A): Linear correlation between the total mass calculated from the Carroucell and the AGIR.

3.6.2. Ethanol/water selectivity:

The selectivity of ethanol over water is strongly related to the hydrophobic/hydrophilic properties of MFI zeolites and then to the Si/Al ratio [30]. Such selectivity ($S_{C_2H_5OH,\,H_2O}$) is defined according to the following equation:

$$S_{C_2H_5OH,\,H_2O} = \frac{{}^{x_{C_2H_5OH}}/_{y_{C_2H_5OH}}}{{}^{x_{H_2O}}/_{y_{H_2O}}} \qquad \textbf{(equation 2)}$$

With *x* and *y,* the molar fractions of a component in the adsorbed and vapor phases, respectively.

The selectivity factor has been determined for increasing ethanol partial pressures (P/P_0 = 0.006-0.52) at water vapor partial pressure P/P_0= 0.16. It is noted that some of the selectivity values are not reported due to uncertainties in the calculated values for the previously studied MFI zeolites. $S_{C_2H_5OH,\,H_2O}$ values are reported in **Figure 8** for Silicalite-1, MFI-45, MFI-25, and MFI-11 for P/P_0 H_2O = 0.16, with an increasing P/P_0 of ethanol. It is observed that the ethanol selectivity decreases with the increase of P/P_0 C_2H_5OH for all the zeolites and is always greater than 1 for Silicalite-1, MFI-45, and MFI-25, suggesting selective ethanol adsorption even at low P/P_0 of C_2H_5OH for the highest silica material. However, the $S_{C_2H_5OH,\,H_2O}$ is lower than 1 for MFI-11 at high ethanol partial pressures indicating preferential water adsorption. Comparing the selectivity between the four samples at a given ethanol partial pressure (for example, at P/P_0 = 0.26) shows that the ethanol sorption selectivity decreases with the Si/Al ratio. Yet, it decreases drastically when comparing Silicalite-1 (**Figure 8 curve (a)**) and MFI-11 (**Figure 8 curve (d)**). Hence, MFI-11, the highest Al content zeolite, is highly selective for adsorbing water over ethanol. It is concluded that the lower the Si/Al ratio, the higher the zeolite hydrophilicity is, and then water is strongly adsorbed in the zeolite and is not easily replaced by ethanol. The effect of the Si/Al ratio on the selectivity of ethanol over water is in agreement with the results reported in the literature [31, 58] , extending this conclusion to larger Si/Al range and at different partial pressures.

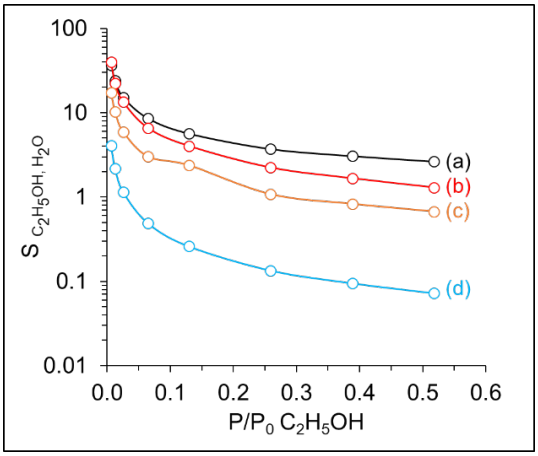

Figure 8: Selectivity of C_2H_5OH determined on Silicalite-1 ((a)-black), MFI-45 ((b)-red), MFI-25 ((c)-orange) and MFI-11 ((d)-light blue) at fixed $P/P_0 = H_2O$ (0.16) and increasing P/P_0 C_2H_5OH.

3.6.3. Influence of the Si/Al and the fraction of H_2O in the gas phase on the relative amount of adsorbed EtOH ($R_{C_2H_5OH}$)

The area of the vibrational band of water at 1630 cm^{-1} cannot always be measured precisely for all zeolites for small amounts of adsorbed H_2O due to the distortion of the baseline in this range (distortion mainly resulting from the shift of the underlying combination and overtone bands of ν_{Si-O} structural vibrations). This is why we have chosen to introduce a new factor independent of the measurement of the quantity of coadsorbed water in order to compare the ethanol adsorption capacities of the overall zeolites with and without water. Hence, the selective adsorption of ethanol is interpreted after introducing a new variable, the ratio of adsorbed ethanol ($R_{C_2H_5OH}$). It is determined as the ratio between the quantity of coadsorbed ethanol ($(Q_{C_2H_5OH})^{P/P_0\ H_2O}_{P/P_0\ C_2H_5OH}$) at a given water and ethanol partial pressures in the presence of water and the quantity of adsorbed EtOH at the same ethanol partial pressure in the absence of water ($(Q_{C_2H_5OH})^{0}_{P/P_0\ C_2H_5OH}$):

$$(R_{C_2H_5OH})_{P/P_0\ C_2H_5OH} = \frac{(Q_{C_2H_5OH})^{P/P_0\ H_2O}_{P/P_0\ C_2H_5OH}}{(Q_{C_2H_5OH})^{0}_{P/P_0\ C_2H_5OH}} \times 100 \quad \textbf{(equation 3)}$$

The ratio of adsorbed ethanol ($R_{C_2H_5OH}$) is plotted as a function of the number of Al atoms per unit cell for different ethanol partial pressures at four different water partial pressures (**Figure 9** and **Figure S6**). For a fixed water vapor concentration, for example, $P/P_0 = 0.16$, the ratio of adsorbed ethanol decreases with the increase of the number of Al per unit cell, regardless of the ethanol partial pressure. At low ethanol partial pressure ($P/P_0 = 0.006$) (**Figure 9 (A)**), the ratio of adsorbed ethanol decreases with the increase of the number of Al for fixed water content. A dramatic difference between the ratios of adsorbed ethanol is observed when the initial water content increases at low ethanol concentrations for a fixed number of Al/unit cell. Nevertheless, this trend is not observed when ethanol concentration is close to saturation ($P/P_0 = 0.52$), although the ratio of adsorbed C_2H_5OH keeps decreasing with the increase of the number of Al per unit cell (**Figure 9 (B)**). This demonstrates the clear effect of water on ethanol adsorption at low pressures and not at high pressures.

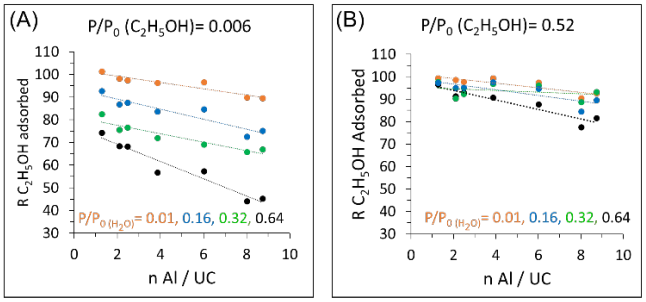

Figure 9: Ratio of adsorbed C_2H_5OH vs the number of Al per unit cell for P/P_0 C_2H_5OH = 0.006 (A) and 0.52 (B) after adsorption of different water partial pressures (P/P_0 H_2O = 0.01 (orange), P/P_0 H_2O = 0.16 (blue), P/P_0 H_2O = 0.32 (green) and P/P_0 H_2O = 0.64 (black)) for different MFI zeolites.

Finally, the ratio of adsorbed C_2H_5OH during the coadsorption of ethanol and water at different ethanol and water partial pressures for all previously studied MFI zeolites is summarized in **Figure 10.** For this, and for each zeolite, a polynomial curve fitting (order 3) has been determined grouping all experimental data ($R_{C_2H_5OH}$ vs % mol H_2O (in gas phase)) in order to reduce the effect of differences in experimental data. The effects of both the Si/Al and the water content in the gas phase are clearly observed on ethanol adsorption. The adsorption of ethanol is less affected by water at low water content. With the increase of the water content in the gas phase, ethanol is less adsorbed, regardless of the Si/Al ratio. Moreover, ethanol is highly adsorbed on high Si/Al ratio zeolites. These results are in good agreement with other studies claiming that the selectivity of ethanol increases with the increase of the Si/Al and the total flux [31, 59]. Therefore, the Si/Al ratio and the water content directly impact the ethanol sorption properties and govern the choice of the mixed membranes to separate bioethanol from its aqueous mixture.

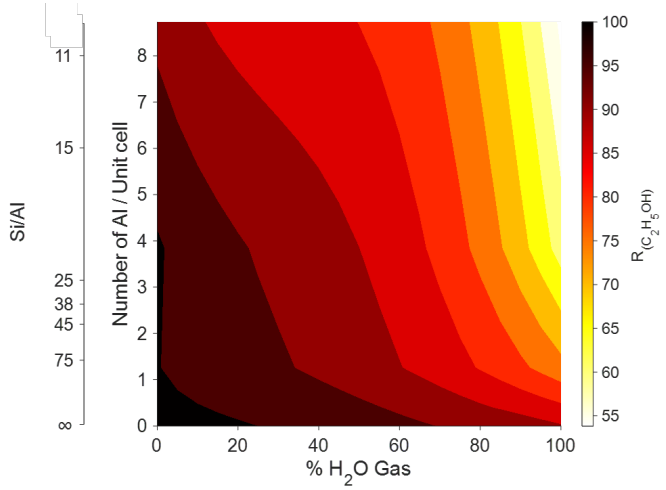

Figure 10: Ratio of adsorbed C_2H_5OH as a function of the number of Al / Unit cell, the Si/Al ratio, and the percentage of H_2O in the gas phase. Note that the adsorption of pure ethanol at 0% H_2O is not included in the figure to avoid mathematical problems in fitting the graph.

Conclusions

The use of advanced vibrational spectroscopic tools allows obtaining quantitative data on ethanol and water adsorption and coadsorption on MFI zeolites with different Si/Al ratios. This quantitative spectroscopic approach leads to the determination of the molar absorption coefficients of adsorbed ethanol and water. They are equal to 0.14 ± 0.01 and 1.29 ± 0.06 cm.µmol^{-1}, respectively and are independent of the Si/Al ratio whether adsorbed or coadsorbed.

Gravimetric-IR coupled experiments reveal that water adsorbs specifically on BAS at low partial pressures, whereas ethanol adsorbs on both silanol and BAS sites. The number of adsorbed molecules per Bronsted acid site is estimated to be four water molecules and two ethanol molecules per site.

The Si/Al ratio effect was further studied and significantly affected ethanol adsorption isotherms only at low partial pressures. However, a significant effect on the amount of adsorbed water is evidenced at extended water partial pressure, illustrating its role on the hydrophobic character of the material.

The use of molar absorption coefficient of adsorbed water and ethanol allows to obtain an important data set relative to the concentration of ethanol and water from the binary adsorption measurements, using the developed multi-sample in-situ IR cell (CARROUCELL). Finally, water molar fraction in the gas phase plays a significant role in ethanol adsorption, leading to lower adsorption capacity at high water content. Furthermore, a higher Si/Al ratio leads to higher ethanol adsorption capacity in the presence of water. This work offers valuable insight into studying other mixtures' adsorption mechanisms using IR spectroscopy.

Author Contributions

The manuscript was written with the contributions of all authors. All authors have approved the final version of the manuscript.

Conflicts of interest

There are no conflicts to declare.

Acknowledgments

R. Zakhia Douaihy acknowledges the Normandy region for the doctoral funding (RIN doctorant). Authors acknowledge Dr. Jaafar El Fallah for helping in the SEM analysis.

References

1. J. J. Cheng and G. R. Timilsina, *Renewable Energy*, 2011, **36**, 3541-3549.
2. V. G. Gude and E. Martinez-Guerra, *Environmental chemistry letters*, 2018, **16**, 327-341.
3. R. Malhotra and L. Das, 2003.
4. S. A. Jambo, R. Abdulla, S. H. M. Azhar, H. Marbawi, J. A. Gansau and P. Ravindra, *Renewable and sustainable energy reviews*, 2016, **65**, 756-769.

5. S. K. Chauhan, S. Gangopadhyay and N. Singh, *Environmental Chemistry Letters*, 2009, **7**, 289-299.
6. S. Karimi, R. R. Karri, M. T. Yaraki and J. R. Koduru, *Environmental Chemistry Letters*, 2021, 1-18.
7. C. R. Soccol, V. Faraco, S. G. Karp, L. P. Vandenberghe, V. Thomaz-Soccol, A. L. Woiciechowski and A. Pandey, in *Biofuels: Alternative Feedstocks and Conversion Processes for the Production of Liquid and Gaseous Biofuels*, Elsevier2019, pp. 331-354.
8. A. S. Kumar, S. S. Sankar, S. Godlaveeti, D. Kumar, S. Dheiver, R. Prasad, C. Nb, T. H. C. Nguyen and Q. Van Le, *Bioenergy Research: Evaluating Strategies for Commercialization and Sustainability*, 2021, 175-208.
9. T. J. Tse, D. J. Wiens and M. J. Reaney, *Fermentation*, 2021, **7**, 268.
10. S. Karimi, M. T. Yaraki and R. R. Karri, *Renewable and Sustainable Energy Reviews*, 2019, **107**, 535-553.
11. S. Kumar, N. Singh and R. Prasad, *Renewable and Sustainable Energy Reviews*, 2010, **14**, 1830-1844.
12. X. Liu, D. Hu, M. Li, J. Zhang, Z. Zhu, G. Zeng, Y. Zhang and Y. Sun, *Journal of Applied Polymer Science*, 2015, **132**.
13. M. El-Roz, P. Bazin, T. B. Čelič, N. Z. Logar and F. Thibault-Starzyk, *Journal of Physical Chemistry C*, 2015, **119**, 22570-22576.
14. S. Mintova, J.-P. Gilson and V. Valtchev, *Nanoscale*, 2013, **5**, 6693-6703.
15. N. Kosinov, J. Gascon, F. Kapteijn and E. J. Hensen, *Journal of Membrane Science*, 2016, **499**, 65-79.
16. L. Bacakova, M. Vandrovcova, I. Kopova and I. Jirka, *Biomaterials science*, 2018, **6**, 974-989.
17. M. Moshoeshoe, M. S. Nadiye-Tabbiruka and V. Obuseng, *Am. J. Mater. Sci*, 2017, **7**, 196-221.
18. J. A. Delgado, M. A. Uguina, J. L. Sotelo, V. I. Águeda, A. García and A. Roldán, *Chemical Engineering Journal*, 2012, **180**, 137-144.
19. J. Laksmono, I. Pratiwi, M. Sudibandriyo, A. Haryono and A. H. Saputra, Kinetic studies of adsorption in the bioethanol dehydration using polyvinyl alcohol, zeolite and activated carbon as adsorbent, 2017.
20. M. Simo, S. Sivashanmugam, C. J. Brown and V. Hlavacek, *Industrial & Engineering Chemistry Research*, 2009, **48**, 9247-9260.
21. J. I. Siepmann, P. Bai and M. Tsapatsis, *Zeolites for separation of ethanol and water*, Univ. of Minnesota, Minneapolis, MN (United States)2018.
22. H. Zhou, J. Mouzon, A. Farzaneh, O. N. Antzutkin, M. Grahn and J. Hedlund, *Langmuir*, 2015, **31**, 8488-8494.
23. R. F. DeJaco, P. Bai, M. Tsapatsis and J. I. Siepmann, *Langmuir*, 2016, **32**, 2093-2101.
24. K. Zhang, R. P. Lively, M. E. Dose, L. Li, W. J. Koros, D. M. Ruthven, B. A. McCool and R. R. Chance, *Microporous and mesoporous materials*, 2013, **170**, 259-265.
25. S.-i. Furukawa, K. Goda, Y. Zhang and T. Nitta, *Journal of chemical engineering of Japan*, 2004, **37**, 67-74.
26. Q. Shi, Z. He, K. M. Gupta, Y. Wang and R. Lu, *Journal of Materials Science*, 2017, **52**, 173-184.
27. K. Alexopoulos, M.-S. Lee, Y. Liu, Y. Zhi, Y. Liu, M.-F. o. Reyniers, G. B. Marin, V.-A. Glezakou, R. Rousseau and J. A. Lercher, *The Journal of Physical Chemistry C*, 2016, **120**, 7172-7182.
28. D. Bastani, N. Esmaeili and M. Asadollahi, *Journal of Industrial and Engineering Chemistry*, 2013, **19**, 375-393.
29. J. Pérez Pariente and M. Martínez Sánchez, 2011.
30. P. Gómez-Álvarez, E. G. Noya, E. Lomba, S. Valencia and J. o. Pires, *Langmuir*, 2018, **34**, 12739-12750.
31. K. Zhang, R. P. Lively, J. D. Noel, M. E. Dose, B. A. McCool, R. R. Chance and W. J. Koros, *Langmuir*, 2012, **28**, 8664-8673.
32. D. Olson, W. Haag and W. Borghard, *Microporous and Mesoporous Materials*, 2000, **35**, 435-446.
33. V. I. Volkov, V. D. Skirda, E. N. Vasina, S. A. Korotchkova, H. Ohya and K. Soontarapa, *Journal of Membrane Science*, 1998, **138**, 221-225.
34. V. I. Volkov, S. A. Korotchkova, H. Ohya and Q. Guo, *Journal of membrane science*, 1995, **100**, 273-286.
35. F. Dreisbach, H. W. Lösch and K. Nakai, *Chemical engineering & technology*, 2001, **24**, 1001-1005.
36. A. Vjunov, M. Wang, N. Govind, T. Huthwelker, H. Shi, D. Mei, J. L. Fulton and J. A. Lercher, *Chemistry of Materials*, 2017, **29**, 9030-9042.
37. A. Zecchina, S. Bordiga, G. Spoto, D. Scarano, G. Spanò and F. Geobaldo, *Journal of the Chemical Society, Faraday Transactions*, 1996, **92**, 4863-4875.
38. V. Zholobenko, C. Freitas, M. Jendrlin, P. Bazin, A. Travert and F. Thibault-Starzyk, *Journal of Catalysis*, 2020, **385**, 52-60.
39. L. Lakiss, I. Yordanov, G. Majano, T. Metzger and S. Mintova, *Thin solid films*, 2010, **518**, 2241-2246.
40. S. Jolly, J. Saussey, M. Bettahar, J. Lavalley and E. Benazzi, *Applied catalysis A: general*, 1997, **156**, 71-96.
41. Z. Qin, L. Lakiss, L. Tosheva, J. P. Gilson, A. Vicente, C. Fernandez and V. Valtchev, *Advanced Functional Materials*, 2014, **24**, 257-264.
42. P. Bazin, A. Alenda and F. Thibault-Starzyk, *Dalton Transactions*, 2010, **39**, 8432-8436.
43. M. Thommes, K. Kaneko, A. V. Neimark, J. P. Olivier, F. Rodriguez-Reinoso, J. Rouquerol and K. S. Sing, *Pure and applied chemistry*, 2015, **87**, 1051-1069.
44. F. Thibault-Starzyk, A. Vimont and J.-P. Gilson, *Catalysis today*, 2001, **70**, 227-241.
45. P. Peng, D. Stosic, A. Aitblal, A. Vimont, P. Bazin, X.-M. Liu, Z.-F. Yan, S. Mintova and A. Travert, *ACS Catalysis*, 2020, **10**, 6822-6830.
46. S. Khabtou, T. Chevreau and J. Lavalley, *Microporous Materials*, 1994, **3**, 133-148.
47. P. O. Fritz and J. H. Lunsford, *Journal of Catalysis*, 1989, **118**, 85-98.
48. Z. Wu, C. Zhang, L. Peng, X. Wang, Q. Kong and X. Gu, *ACS applied materials & interfaces*, 2018, **10**, 3175-3180.
49. M. Selvaraj and F. Banat, in *Biorefinery*, Springer2019, pp. 211-232.
50. F. Thibault-Starzyk, I. Stan, S. Abelló, A. Bonilla, K. Thomas, C. Fernandez, J.-P. Gilson and J. Pérez-Ramírez, *Journal of Catalysis*, 2009, **264**, 11-14.
51. P. A. Jacobs and C. Heylen, *Journal of Catalysis*, 1974, **34**, 267-274.
52. L. M. Parker, D. M. Bibby and G. R. Burns, *Zeolites*, 1993, **13**, 107-112.
53. G. Piccini, M. Alessio and J. Sauer, *Physical Chemistry Chemical Physics*, 2018, **20**, 19964-19970.
54. D. Wu, X. Guo, H. Sun and A. Navrotsky, *The Journal of Physical Chemistry C*, 2015, **119**, 15428-15433.

55. A. Jentys, G. Warecka, M. Derewinski and J. A. Lercher, *The Journal of Physical Chemistry*, 1989, **93**, 4837-4843.
56. V. Bolis, C. Busco and P. Ugliengo, *The Journal of Physical Chemistry B*, 2006, **110**, 14849-14859.
57. D. Olson, S. Zygmunt, M. Erhardt, L. Curtiss and L. Iton, *Zeolites*, 1997, **18**, 347-349.
58. K. Ueno, H. Negishi, M. Miyamoto, S. Uemiya and Y. Oumi, *Microporous and Mesoporous Materials*, 2018, **267**, 1-8.
59. X. Zhan, J.-d. Li, J. Chen and J.-q. Huang, *Chinese Journal of polymer science*, 2009, **27**, 771-780.